



### **Science Arts & Métiers (SAM)**

is an open access repository that collects the work of Arts et Métiers Institute of Technology researchers and makes it freely available over the web where possible.

This is an author-deposited version published in: <https://sam.ensam.eu>  
Handle ID: <http://hdl.handle.net/10985/11097>

#### **To cite this version :**

Benjamin GERIN, Catherine VERDU, Alain MARY, Franck MOREL, Etienne PESSARD -  
Beneficial effect of prestrain due to cold extrusion on the multiaxial fatigue strength of a 27MnCr5  
steel - International Journal of Fatigue n°92, p.345-359 - 2016

Any correspondence concerning this service should be sent to the repository

Administrator : [scienceouverte@ensam.eu](mailto:scienceouverte@ensam.eu)



# Beneficial effect of prestrain due to cold extrusion on the multiaxial fatigue strength of a 27MnCr5 steel

Benjamin Gerin<sup>a,b,\*</sup>, Etienne Pessard<sup>a</sup>, Franck Morel<sup>a</sup>, Catherine Verdu<sup>b</sup>, Alain Mary<sup>c</sup>

<sup>a</sup> LAMPA, Arts et Métiers ParisTech Angers, 2 Bd du Ronceray, 49035 Angers Cedex 01, France

<sup>b</sup> MATEIS, INSA de Lyon, Bâtiment St Exupéry, 20 av Jean Capelle, 69621 Villeurbanne Cedex, France

<sup>c</sup> Gevelot, 94 rue Saint-Melaine BP 0409, 53004 Laval Cedex, France

Keywords:

Steel

Forging

Prestrain

High cycle fatigue

Multiaxial criterion

## A B S T R A C T

Cold extrusion is a process commonly used to manufacture drive train components in the automotive industry. Large plastic strains can be applied during this operation (up to 1.5) and greatly changes the mechanical properties of the resulting material. This study focuses on the impact of cold extrusion process parameters on the multiaxial fatigue behaviour of steel components. A specific set of forward rod extrusion tools was developed to get original fatigue specimen able to characterise the effect of the manufacturing process on the fatigue behaviour. The specimens were extruded from two different initial diameters, giving two different reductions in cross-section of 18% and 75% respectively.

To understand the influence of cold extrusion, the following analyses have been undertaken for each condition and on the initial material: monotonic tensile properties, microstructure, EBSD, residual stresses and hardness. Simulation of the forming process and microstructural observations show that the plastic strain is homogeneous in the specimen section. For both reduction factors, the forming process has a positive effect on the components properties: induced residual stresses in compression and improved hardness and roughness ( $R_a$  decreasing). Tension, plane bending and torsion fatigue tests show that the fatigue strength is about 30% higher for the batch with 75% reduced cross-section. All investigations show that strain hardening is the principal material parameter responsible for the increase in fatigue strength. A multiaxial fatigue criterion taking into account the effects of the forward rod extrusion process was also developed.

## 1. Introduction

Cold extrusion is a very common process for manufacturing automobile parts through plastic strain. This process requires very expensive dies, and is thus mainly used for mass production, most notably for drive train components. The steering rack pivot shown in Fig. 1 is an example of the type of component manufactured with this process. Areas with different strain levels can be seen along the component.

This process has many advantages, achieving high production speeds (from 10 to over 100 parts per minute), tight tolerances (a few hundredths of millimetres) and high quality surface states ( $R_a$  values as low as 0.5  $\mu\text{m}$ ), as shown by Pale et al. [22].

From a material science perspective, the principal effects of the plastic strain is the hardening of the material, the introduction of residual stresses and in some cases damaging the material.

Many articles in the literature study the effect of a prestrain generated by service loading on the low cycle fatigue behaviour Feltner and Laird [6], Kunz et al. [13], Wang et al. [35], Marnier et al. [15]. However, few studies focus on the high cycle fatigue. The goal of these studies is often to estimate the fatigue strength of the component, following a voluntary or accidental plastic strain (proof load). In these studies, the prestrain direction and the loading direction during the fatigue tests are always the same. The effect of the prestrain on fatigue strength depends on the intensity of the applied prestrain and on the type of material being tested. For example, Froustey and Lataillade [7] studied two aluminium alloys, showing that an aluminium-copper alloy is highly sensitive to prestraining, while an aluminium-magnesium is insensitive to it. They also showed that changing the strain rate of the prestrain had no influence. Zimmermann et al. [36] studied a nickel-based alloy and a martensite-forming austenitic steel. They found that

\* Corresponding author at: LAMPA, Arts et Métiers ParisTech Angers, 2 Bd du Ronceray, 49035 Angers Cedex 01, France.

E-mail address: benjamin.gerin@ensam.eu (B. Gerin).



Fig. 1. Example of a forged component: a steering rack pivot, showing multiple reductions of the cross-section. Photo credit: Gevelot Company.

prestrain improved the fatigue strength for the steel, but not for the nickel-based alloy. Nagase and Suzuki [21] show that on a low carbon steel, a small 0.03 plastic strain tends to lower the fatigue limit, whereas a higher 0.06 strain improves it. Kang et al. [12] have also observed that a prestrain can be beneficial in fatigue for a low carbon steel, but negative for a quenched C50 steel.

Concerning the impact of the prestrain generated during the forming process on the fatigue behaviour, the few articles in the literature focus on cold-rolling of sheets and plates [29], or on cold drawing of wires [34]. Cold drawing of wires is the process closest to cold extrusion because the strain applied in the two processes are similar, with high axisymmetric strain. Most studies on cold drawing, such as Beretta and Boniardi [1], analyse the effects of the process on the microstructure and on the fatigue strength of the material, specifically the crack propagation threshold. The wires commonly have a very high yield stress after drawing (over 1500 MPa), and often the crack initiation is located on surface defects. To predict the fatigue strength, these authors suggest an approach based on the Linear Fracture Mechanics, where the defect is considered as a pre-existing crack, as seen in Murakami [20].

A major study of the influence of prestrain on fatigue behaviour is the work done by Munier [18], Munier et al. [19]. Using self-heating tests to estimate the fatigue strength at  $10^6$  cycles, Munier studied the influence of various amounts of prestrain (from 0.01 to 0.30) on the fatigue behaviour of multiple grades of steel. The study also compares the effect of different prestrain loading such as uniaxial tension, plane stress tension and shearing; the influence of the direction of the prestrain compared to the fatigue loading is also discussed. Munier's results show that for all grades of steel and all prestrain conditions, the fatigue behaviour is negatively affected for small values of prestrain, reaching a minimum before increasing and eventually exceeding the base fatigue strength for higher amounts of prestrain. The minimum amount of prestrain required to exceed the base fatigue strength varies depending on the material and the prestrain conditions, ranging from less than 0.05 to over 0.25. The minimum fatigue strength also varies, but is lowest for the cases where a large amount of prestrain is required to exceed the base fatigue strength. In these cases, the minimum fatigue strength is as low as 80% of the base strength. However, the range of prestrain values investigated is much smaller than what is typical in cold-forging.

There are few studies where the effects of high prestrain are analysed. One such study was performed by Libertiny et al. [14], on a mild steel and a high-strength low-alloy steel. Two types of prestrain were studied: tension prestrain, and reducing the specimen thickness through cold-rolling. The tension prestrain applied was 90% or 95% of the fracture strain in tension. The rolling was used to reduce the specimen thickness to 62% of the initial area. Fatigue tests in tension were performed to determine the fatigue strength at  $10^6$  cycles. For the mild steel, the 90% prestrain improves the fatigue strength by 50%, and the rolling by 100%. For the high-strength steel, the prestrain equal to 90% of the fracture strain yields a 40% improvement. However, for both materials the prestrain equal to 95% of the fracture strain did not improve the fatigue strength.

These articles Munier [18], Munier et al. [19], Libertiny et al. [14], Froustey and Lataillade [7], Zimmermann et al. [36] show that a large number of parameters associated with prestrain can affect the fatigue behaviour:

- The type the prestrain loading (uniaxial tension, plane strain tension, shearing, etc.).
- The intensity of the prestrain.
- A heat-treatment applied after the prestrain.

In addition, the observed fatigue behaviour also depends on the testing conditions, with the results depending on:

- The direction of the fatigue loading compared to that of the prestrain loading.
- The type of fatigue test being performed (controlled stress or strain, loading mode, load ratio, etc.).
- The fatigue regime being investigated (low or high cycle fatigue).

The study presented in this article is part of the French national research project DERSURF, with industrial partners ranging from the steel producer to the car manufacturer. The study was performed on specimens that are representative of industrial components obtained by cold extrusion. The plastic strain applied during the forward rod extrusion process comes from a reduction of the cross-section of the component, and is therefore mainly compressive.

Firstly, Finite Element simulations of the extrusion were performed to estimate the heterogeneity of the plastic strain in the specimens. Secondly, an in-depth analysis of the effects of the cold extrusion process on microstructure, mechanical characteristics and fatigue strength was conducted. The fatigue tests will be performed in three loading conditions: tension, bending and torsion. The goal of these fatigue tests was threefold. First, the results were used to quantify the influence of prestrain on fatigue behaviour. Second, both the core material (tension tests) and the forged surface (bending) were tested and compared. The applied loading during these fatigue tests was uniaxial and in the longitudinal direction (extrusion direction) of the specimens. Third, tension and bending tests combined with the torsion tests were used to identify a multiaxial fatigue criterion.

The specimens were designed in collaboration with, and manufactured by, the Gévelot company. The geometry was based on cold-forged industrial components (Fig. 1). The specimens are extruded from a round bar of 27MnCr5 steel, leading to a reduction of the cross-section after extrusion. To investigate the impact of this reduction, two different cross-section reductions were chosen, representing the two extremes in forward rod extrusion as applied in the Gevelot Company: the smallest reduction always applied, and the largest reduction possible without risking damaging the component. These are respectively 18% and 75% reduction of the cross-section (above 75%, classical ductile steels used in cold-forging can show damage such as tearing during forming). The corresponding minimum true strain values, given by  $\ln(A_0/A_{\text{mini}})$ , are

respectively 0.20 and 1.40. To obtain the same final specimen diameter of 13.55 mm, the 27MnCr5 steel bars were machined to two different initial diameters (15 and 27.4 mm). An image of the initial billets and the forged specimens is given in Fig. 2. The specimen head is left unforged, and is machined after extrusion in order for all specimen to have the same geometry. The specimen geometry is given in Fig. 3. Because all of the fatigue specimens were machined out of the forged specimens, it was not possible to use standard dimensions for the fatigue specimens.

The fatigue specimens were polished to a mirror finish after machining, except in the case of the bending specimens, where the surface was left as-forged. The two batches will be referred to as 18% reduced cross-section and 75% reduced cross-section. The initial material will be referred to as before extrusion.



Fig. 2. Photograph showing the billet and the forged specimen, for both batches. Left: 75% reduced cross-section. Right: 18% reduced cross-section. The specimen heads are not yet machined. Photo credit: Gevelot Company.

It should be noted that, according to the industrial process, the material has been annealed prior to forging to increase its ductility. Fig. 4 shows the various steps for the forging and the preparation of the specimens, from hot-rolling of the initial bar to fatigue testing.

## 2. Simulation of the forward rod extrusion process

Simulation of the forward rod extrusion was performed with the finite element simulation software Forge2011<sup>®</sup>. The first goal of this numerical study is to predict the heterogeneity of the plastic strain introduced during extrusion using the results of the simulations. The second goal is to showcase the possibility of predicting certain material properties after extrusion, such as hardness. These predictions could then be used in the design phase of components to predict fatigue strength, for example.

The computation is performed using a 2D axisymmetrical configuration. A 3D representation of the cold extrusion process is presented in Fig. 5a. The element size is about 0.5 mm in the core and 0.25 mm at the surface (Fig. 5b).

A Hansel & Spittel elasto-visco-thermo-plastic law is used for the specimen, in the plastic domain the stress is expressed as:

$$\sigma = A e^{m_1 T} \dot{\epsilon}_p^{m_2} e^{m_3 / \sqrt{\dot{\epsilon}_p}} \dot{\epsilon}_p^{m_4} \quad (1)$$

where the  $m_1$  parameter controls the influence of the temperature,  $m_2$  is the strain-hardening coefficient,  $m_3$  is the influence of the strain-rate and  $m_4$  controls the shape of the strain-hardening. The  $m_1$  and  $m_3$  parameters were set to the classical values used for steels, and the  $A$ ,  $m_2$  and  $m_4$  parameters were determined experimentally using compression tests on the material. Table 1 lists the values for all parameters. The tools are considered perfectly rigid and have the exact same dimensions as the tools designed by the Gevelot Company for this study. The punch speed is  $20 \text{ mm s}^{-1}$ . The friction at each interface is modelled using a Coulomb law limited by a Tresca threshold, with parameters  $\mu = 0.03$  and  $m = 0.07$ . These are classical values for the zinc phosphate coating and soap-

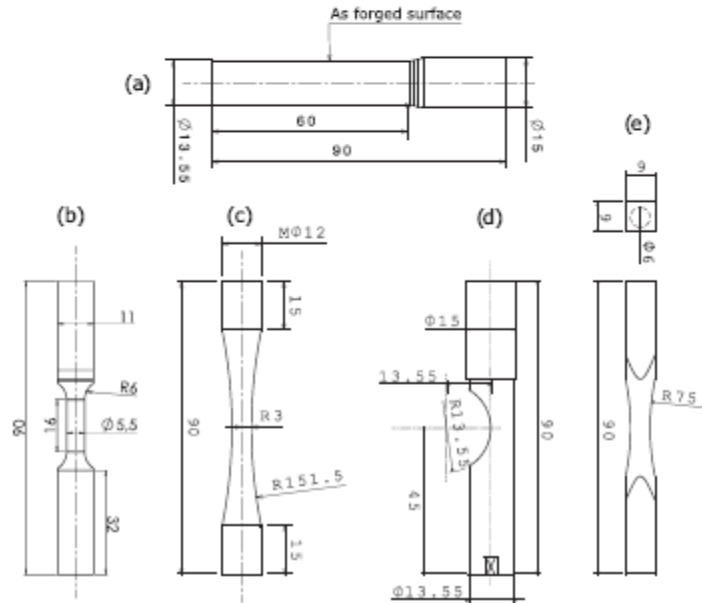


Fig. 3. Geometries of the specimens. All units are in mm. (a) As-forged specimen, the head of the specimen remains unforged. All other specimens are machined out of this geometry. (b) Monotonic tensile test specimen. (c) Tension fatigue specimen. (d) Bending fatigue specimen. (e) Torsion fatigue specimen.

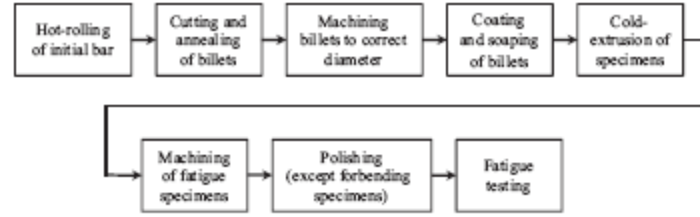


Fig. 4. The various steps for the forging and the preparation of the specimens.

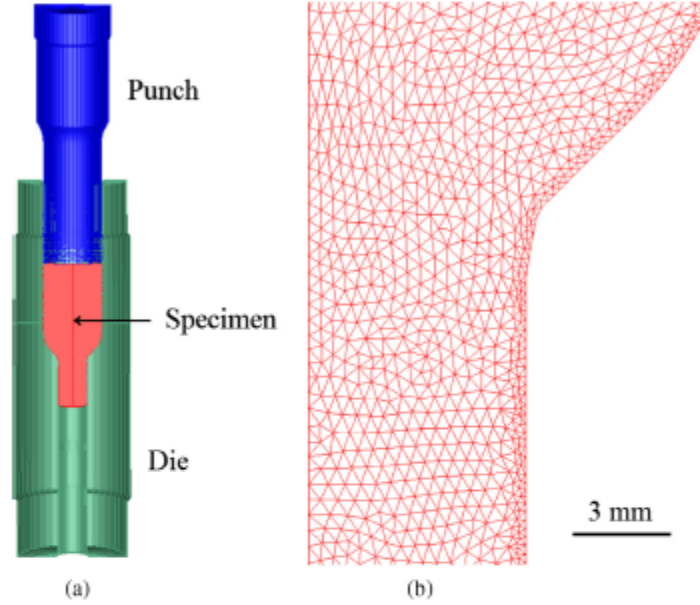


Fig. 5. (a) 3D representation of the 2D axisymmetrical simulation of the forward rod extrusion process. (b) Mesh in the area with the highest strain.

Table 1  
Parameters for the Hansel & Spittel law of the 27MnCr5 material used in the FE simulations.

Parameter	A	$m_1$	$m_2$	$m_3$	$m_4$
Value	1010	-0.0009	0.138	0.00988	-0.005

ing process used in the cold-forging of steel [8]. The solution algorithm is explicit, with complex elements based on C3D4 elements; however, the element and algorithm formulations are not the focus of this study. As such, a detailed explanation concerning the simulation, mini-element formulation, the contact and resolution algorithms and the remesher can be found in a paper by Bouchard et al. [2].

The results of the FE simulations are given in Fig. 6. The geometry of the specimen is correctly predicted, in particular the convex tip of the 75% reduced cross-section specimen is clearly visible in the simulation. The Von Mises equivalent plastic strain is quite homogeneous for both conditions, ranging from 0.2 to 0.4 for the 18% reduced cross-section specimens, and from 1.4 to 1.7 for the 75% specimens. For both specimens, the plastic strain is lowest at the centre of the specimen, and highest just below the surface. The principal plastic strain tensor in the centre of the specimen is:

$$\begin{aligned}
 &18\% \text{ reduced cross-section: } \varepsilon^p = \begin{pmatrix} 0.204 & 0 & 0 \\ 0 & -0.100 & 0 \\ 0 & 0 & -0.104 \end{pmatrix} \\
 &75\% \text{ reduced cross-section: } \varepsilon^p = \begin{pmatrix} 1.40 & 0 & 0 \\ 0 & -0.69 & 0 \\ 0 & 0 & -0.71 \end{pmatrix}
 \end{aligned}$$

The first principal plastic strain has the same orientation as the specimen axis (long direction).

To predict the final hardness of the specimens, the Forge2011® software uses an empirical law linking the Vickers hardness to the equivalent Von Mises stress:  $H_V = \frac{\sigma_{\text{Mises}}}{3}$ . This law is based on the work done by Tabor [31], showing a link between yield stress and hardness, used in many other articles like Tekkaya and Lange [32]. During the simulation, plastic strain leads to hardening which changes the yield stress. As an approximation of the yield stress, the software uses the maximum Von Mises stress. At each time step, the software uses the maximum Von Mises stress for each element to evaluate the local hardness, and updates the value if it is higher than the hardness at the previous time step. The initial hardness is set at 164 Hv and was measured experimentally.

Some authors suggest another method, which was not used in this study, using strain-hardening reference curves in the

simulation to obtain a more accurate hardness prediction. These curves are obtained by analysing a compression test on a cylinder. In the case of cold-forged components, a number of authors, such as Sonmez and Demir [30], show that it is now possible to accurately predict the component's hardness after extrusion with this method.

Results show that the hardness for the 18% reduced cross-section specimen follows the same general gradient as the plastic strain, ranging from 250 to 275 HV. For the 75% reduced cross-section specimen, the hardness is very homogeneous, at 300 HV. The hardness is more homogeneous than the plastic strain because it is calculated using the equivalent stress and not the strain. The shape of the Hansel & Spittel law means that an increase in strain will only lead to a relatively small increase in stress.

### 3. Mechanical properties and microstructural characteristics under the different extrusion conditions

The specimens are made from cold-working round bars of 27MnCr5 ferrite-pearlite steel (see Table 2 for chemical composition). The bars are machined to the correct dimensions before extrusion. To quantify the effects of the process, tensile tests were performed on the heat-treated material before and after extrusion.

The specimen geometry for the monotonic tensile tests is shown in Fig. 3. The tensile test specimens do not have standard dimensions because they were machined out of the extruded specimens. Furthermore, few tensile tests were performed so as to keep as many specimens as possible for the fatigue tests. The tests were strain-controlled with strain rate of  $0.001 \text{ s}^{-1}$ . The stress-strain curves are given in Fig. 7, and the mechanical characteristics are given in Table 3. Combined with hardness tests (Fig. 8), these show

Table 2  
Chemical composition of the 27MnCr5 steel, in weight percentage.

Element	C	Mn	Cr	Si	S	Ni	Cu
Min	0.240	1.100	1.000		0.0200		
Actual	0.266	1.193	1.080	0.234	0.0313	0.106	0.109
Max	0.270	1.400	1.120	0.300	0.0330	0.250	0.250

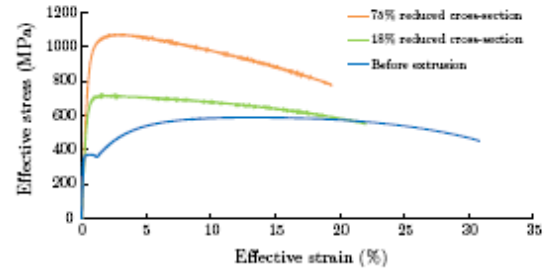


Fig. 7. Stress-strain curves of the material before and after extrusion.

how the hardening introduced during cold-working has changed the material properties. The more the material has been deformed, the more the hardness increases, as well as the yield stress and ultimate stress.

The impact of the hardening is most noticeable on the microstructure of the specimens (Fig. 9). All show alternating bands of ferrite and pearlite, generated during the hot-rolling of the initial bar. These bands explain the variations in hardness

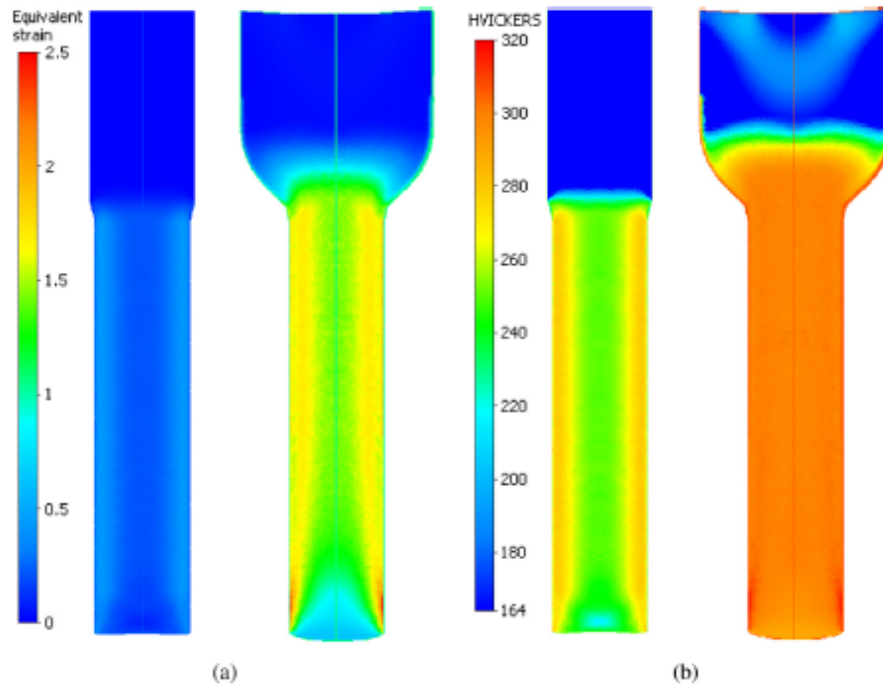


Fig. 6. FE simulations of the forward rod extrusion process, showing in cross-section (a) the equivalent plastic strain and (b) the hardness. For each result, the 18% reduced cross-section specimen is on the left and the 75% reduced cross-section specimen is on the right. The top parts of the specimens are not extruded, showing the two different reductions in cross-section.

Table 3  
Mechanical characteristics of the 27MnCr5 steel, before and after extrusion.

Characteristic	$\sigma_{YS}$ (MPa)	$\sigma_{UTS}$ (MPa)	$A_5$ (%)	Hardness $H_V$ 0.3 kg average $\pm$ std. dev.	Simulated hardness $H_V$
Before extrusion	369	590	31	$164 \pm 10$	–
18% reduced cross-section	614	727	22	$233 \pm 13$	250–275
75% reduced cross-section	886	1075	19	$288 \pm 15$	300

observed in Fig. 8. For the 18% reduced cross-section specimen, the microstructure is visually similar to that of the material prior to extrusion. The bands have an average width of around 20  $\mu\text{m}$ . However for the 75% reduced cross-section specimen, the microstructure has been completely altered. The grains have been stretched in the extrusion direction, and the ferrite and pearlite bands are much thinner and shorter, with an average width of around 10  $\mu\text{m}$  (Fig. 9).

Electron back-scattering (EBSD) maps were acquired on the cross-section of the specimens. EBSD gives a visual representation of the ferrite grain orientations, showing the impact of the extrusion on the grains. Characterization was performed on a Zeiss Supra VP55 SEM with a field-emission gun, operated at 15 kV and equipped with an Oxford-Instruments EBSD camera. A step size of 0.5  $\mu\text{m}$  was used for the before extrusion and 18% reduced cross-section specimens, while 0.3  $\mu\text{m}$  was used for the 75% specimen. Fig. 10 shows the Inverse Pole Figure (IPF) maps for the three batches. It should be noted that the cementite is not visible in the maps, meaning that only the ferrite grains in the ferrite and pearlite

bands are mapped. The 18% reduced cross-section microstructure is visually indistinguishable from the non-worked microstructure, with equiaxed grains. On the other hand, the 75% reduced cross-section microstructure is very anisotropic, with heavily deformed grains stretched in the extrusion direction. Measuring the grain sizes in the EBSD images confirms that the before extrusion and 18% reduced cross-section microstructures are very similar, and that the grains have changed shape in the 75% reduced cross-section specimens. Mean grain size was calculated assuming a minimum misorientation between two grains of 13°. Table 4 gives the mean grain area, the standard error of the mean grain area and the mean grain aspect ratio. The standard error is calculated by dividing the standard deviation by the square root of the number of samples. The effect of the extrusion process on the grains can also be seen in the pole figures (Fig. 11). These show that the microstructure is isotropic before extrusion, whereas this is no longer the case for the extruded specimens, notably for the 75% reduced cross-section specimen which has a heavily anisotropic microstructure.

Comparing the average hardness to the simulated hardness shows that the values are very close (Table 3). The hardness profile for the 75% reduced cross-section specimen also shows a small hardness gradient, with the hardness at the surface being 30  $H_V$  higher than in the core (Fig. 8). A similar gradient can be seen on the plastic strain results of the FE simulations (Fig. 6), with higher values near the surface. The gradient is not present on the simulated hardness gradient and this shows that a complex hardness model is required to predict more accurately local hardness.

The forward rod extrusion process also introduces residual stresses in the specimens. The residual stresses were analysed using X-ray diffraction. A PROTO iXRD machine was used, equipped with a Cr anode vacuum tube and two PSD detectors.

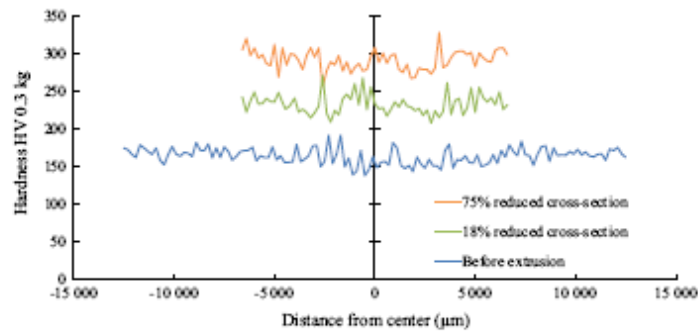


Fig. 8. Hardness of the specimens for each state.  $H_V$  0.3 kg micro-hardness tests, measured in the transverse direction, along the specimen diameter (the core of the specimen is the middle of the curve).

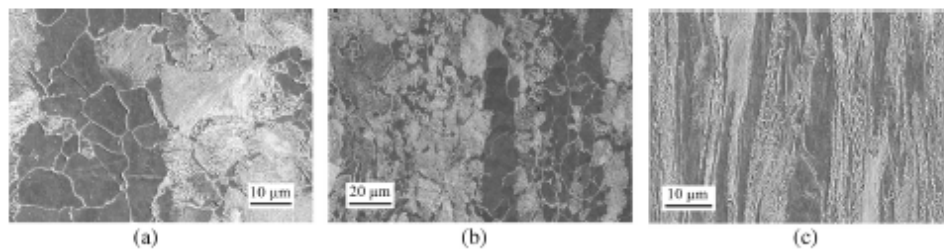


Fig. 9. SEM images taken in the long direction, on the edge of specimens (a) before extrusion, (b) 18% reduced cross-section and (c) 75% reduced cross-section. All show alternating bands of ferrite (gray) and pearlite (white), generated during prior hot-rolling. The hot-rolling direction and the extrusion direction are the same.

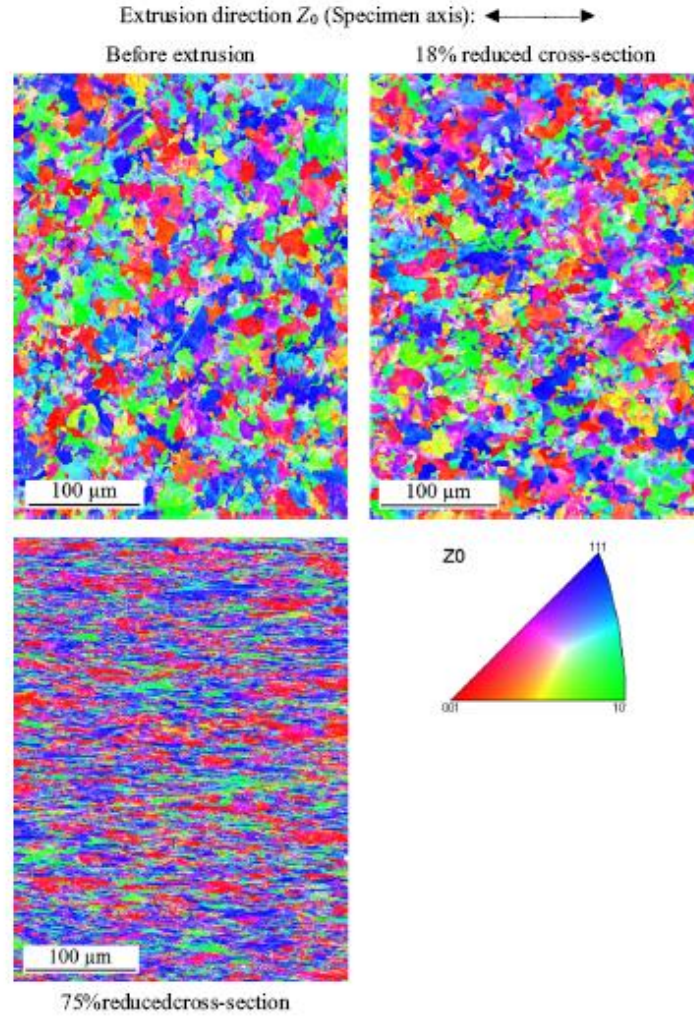


Fig. 10. EBSD IPF maps of the microstructure of the three batches.  $Z_0$  is the extrusion direction.

Table 4

Mean area, standard error of the mean area and mean aspect ratio of the grains for the three states. Sizes measured from EBSD images, with grains smaller than 5  $\mu\text{m}$  ignored.

		Before extrusion	18%	75%
Long direction	Mean area ( $\mu\text{m}^2$ )	85	88	55
	Std. error of the mean area	1.1	2.7	1.9
	Mean aspect ratio	1.93	1.98	6.34
Transverse direction	Mean area ( $\mu\text{m}^2$ )	93	78	33
	Std. error of the mean area	1.4	2.0	0.8
	Mean aspect ratio	1.93	1.92	2.26

The  $K\alpha$  radiation of the Cr target has a wavelength of  $\lambda = 0.22909$  nm. The diffracting planes are the  $\{211\}$  planes of the BCC structure of the ferrite, with a Bragg angle of  $2\theta = 156.4$ . The crystallographic elastic constants used were:  $S_1 = -1.28 \times 10^{-6} \text{ MPa}^{-1}$  and  $\frac{1}{2}S_2 = 5.92 \times 10^{-6} \text{ MPa}^{-1}$ . The first measure is on the surface, with deeper measurements obtained by locally removing thin surface

layers through electropolishing. For the cold-formed specimens, the measurements were made in the middle of the extrudate on the specimens. The residual stresses profiles are shown in Fig. 12. Before extrusion, the machining process has introduced residual stresses near the surface of the specimens, which become close to zero at a depth of around 500  $\mu\text{m}$ . For both extruded batches,

the residual stresses are always compressive at the surface, in both the extrusion direction and the transverse direction. However, in the 18% reduced cross-section specimens, the residual stresses become tensile at the depth of 50  $\mu\text{m}$ . For the 75% reduced cross-section specimens, the residual stresses in the extrusion direction stay compressive even at a depth of 1 mm; whereas in the transverse direction, the residual stresses are close to zero after 100  $\mu\text{m}$ .

Additionally, the forward rod extrusion process improves the surface roughness. 3D surface scans of the specimens were made using a Bruker ContourGT-K0-X profilometer.  $R_a$  roughness values were calculated from 2D profiles extracted from the scans in the longitudinal direction, using a cut-off distance of 800  $\mu\text{m}$ . Before extrusion,  $R_a$  value is 2.5  $\mu\text{m}$  and after extrusion, the  $R_a$  is 1  $\mu\text{m}$  for the 18% reduced cross-section specimen and 0.3  $\mu\text{m}$  for the 75% reduced cross-section specimen.

#### 4. Fatigue behaviour

In order to investigate the effects on fatigue behaviour of the different process parameters, such as surface roughness and pre-strain, fatigue tests were conducted, in tension, bending and tor-

sion. The specimens were machined out of the forged specimens manufactured by the Gévelot Company, the geometries are given in Fig. 3.

Tension fatigue tests with a load ratio of  $R = -1$  on all three batches served to quantify the impact of the prestrain on the fatigue behaviour. The specimens were mirror polished after machining, to remove the milled surface roughness.

To investigate the influence of the forged surface, tension or rotating bending tests were not possible, as that would require machining the specimens in a way that removed the forged surface. Instead, plane bending fatigue tests on both extruded batches were performed. The specimens were machined with a notch in order to have the crack initiate in the middle of the specimen and not in the clamps of the fatigue machine. To avoid crack initiation in the notch, a load ratio of  $R = 0.1$  was used.

Finally,  $R = -1$  torsion fatigue tests were used to analyse the fatigue damage mechanisms under a different loading mode and to identify a Dang Van [4] multiaxial fatigue criterion. The torsion tests were also performed because drivetrain components are frequently loaded in torsion. The specimens were polished after machining as well.

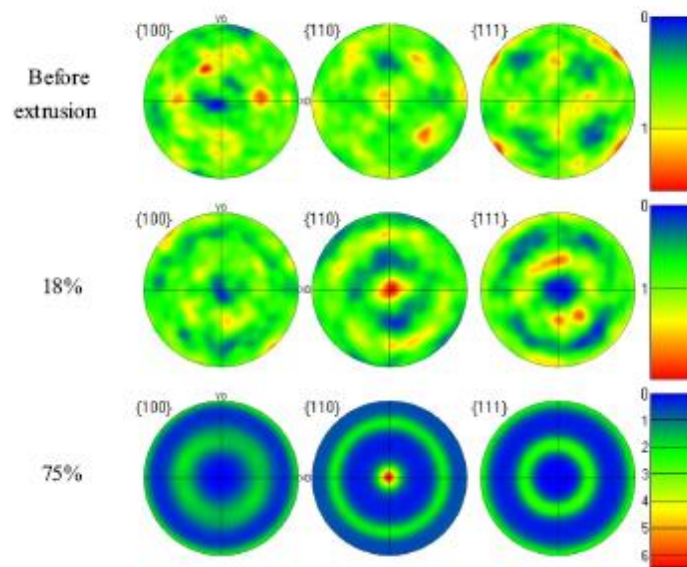


Fig. 11. Pole figures taken in the transverse direction. Scale is point density factor.

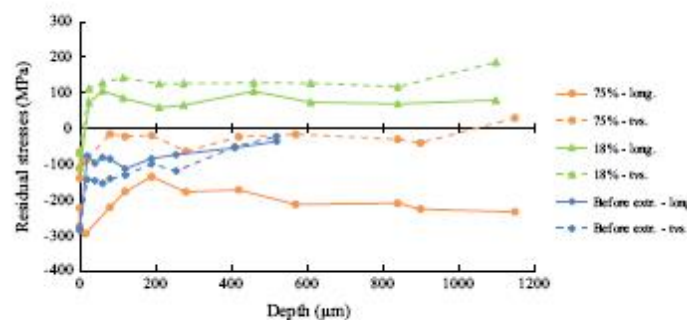


Fig. 12. Residual stresses measured by X-ray diffraction on the as-forged specimens, in the extrusion direction (long) and the transverse direction (Trans).

A staircase method at  $2 \cdot 10^6$  cycles on 10 specimens in tension, 15 in bending and 9 in torsion was performed for each loading condition (the detailed staircases are given in Table 5). The Dixon and Mood [5] staircase method determines the fatigue limit using multiple specimens. The first specimen is cycled with a load close to the expected fatigue limit. If a specimen survives the  $2 \cdot 10^6$  cycles, the loading value is increased for the next specimen. If a specimen fails, loading is decreased for the next specimen. Loading is increased or decreased by a fixed value chosen so as to be small enough to accurately reflect the fatigue dispersion without leading to too many load levels (generally 10–25 MPa). After all specimens have been cycled, a statistical analysis determines the fatigue limit.

The tests were run on two resonant fatigue testing machines, at a frequency of 85 Hz in tension, 80 Hz in bending and 88 Hz in torsion. Specimen failure was determined by the presence of a crack, indicated by a decrease of the resonant frequency. The tests were stopped when the frequency dropped by 0.5 Hz. To observe the crack fracture surface, the specimens were then manually broken after being submerged in liquid nitrogen.

Only 3 specimens were available for the torsion tests on the 18% reduced cross-section specimens. Therefore, instead of a staircase

for this batch, tests were performed using the “step” technique detailed by Maxwell and Nicholas [16]. Each specimen was loaded with a series of constant stress amplitude loading steps. The initial stress amplitude was chosen to be slightly less than the expected fatigue strength at  $2 \cdot 10^6$  cycles. If the specimen did not fail in less than  $2 \cdot 10^6$  cycles, the stress amplitude was increased for the following step. This was repeated until the specimen failed in less than  $2 \cdot 10^6$  cycles. The fatigue strength was then assumed to be the applied stress amplitude of the final step. The overall fatigue strength for the batch was assumed to be the average of the three values.

To monitor the evolution of the residual stresses in the bending specimens, measurements on the surface were also made after machining and after cycling (on surviving specimens), given in Table 6. The detail of every residual stress measurement on surviving bending specimens is given in Table 7. These show that the surface residual stresses change very little for the 75% reduced cross-section specimens. However the surface residual stresses in the 18% reduced cross-section double after machining. This is likely due to the relaxation of the tensile residual stresses during the machining of the notch.

**Table 5**  
Results of the various staircase tests. “O” means surviving specimen, “X” means failure.

Tension $R = -1$	$\sigma_e$ (MPa)	Specimen number														
		1	2	3	4	5	6	7	8	9	10					
Before extrusion	260		X		X		X									
	250	O		O		O		X		O						
	240								O							
18%	315	X				X		X								
	300		X		O		O		X							
	285			O												
75%	485							X		X						
	465		X				O		O		X					
	450	O		X		O										
	435				O											
Bending $R = 0.1$	$\sigma_e$ (MPa)	Specimen number														
		1	2	3	4	5	6	7	8	9	10	11	12	13	14	15
18%	342	X														
	324		X		X		X		X				X			
	306			O		O		O		X		O		X		O
	288										O				O	
75%	468									X				X		
	450						X		O		X		O		X	
	432	X				O		O				O				X
	414		X		O											
	396			O												
Torsion $R = -1$	$\sigma_e$ (MPa)	Specimen number														
		1	2	3	4	5	6	7	8	9						
Before extrusion	195				X		X									
	185			O		O			X		O					
	175		O							O						
75%	340		X													
	325			X		X				X		X				
	310					O		X					X			
	295								O		O					

**Table 6**  
Surface residual stresses measured by X-ray diffraction in the various states of the bending fatigue specimens, in the extrusion direction. The after cycling value is the average of all surviving staircase specimens.

	As-forged (MPa)	Machined (MPa)	After cycling (MPa)
18% reduced cross-section	−100	−220	−193
75% reduced cross-section	−300	−270	−288

Table 7

Surface residual stresses measured by X-ray diffraction in all the surviving bending staircase specimens. The longitudinal direction (long.) is the extrusion direction and the transverse direction (trans.) is the perpendicular.

Bending	18% reduced cross-section				75% reduced cross-section			
	N°	$\sigma_e$	$\sigma_{Res}$ (MPa)		N°	$\sigma_e$	$\sigma_{Res}$ (MPa)	
			Long.	Trans.			Long.	Trans.
	3	306	-127	-135	3	396	-238	-201
	5	306	-150	-165	4	414	-311	-215
	7	306	-197	-217	5	432	-310	-220
	10	288	-226	-220	7	432	-294	-172
	11	306	-249	-150	8	450	-247	-224
	14	288	-191	-146	11	432	-302	-181
	15	306	-212	-159	12	450	-320	-191
Average			-193	-170			-288	-201
Range			85	85			82	52

During fatigue testing the macroscopic bending loading leads to plastic strain on the surface and the introduction of residual stresses. The local surface stress loading is therefore different from the applied  $R = 0.1$  loading. The plastic strain was verified using strain gauges: the maximum plastic strain is 0.6% for the 75% reduced cross-section specimens and 0.4% for the 18% reduced cross-section specimens. The stabilised loading cycles is reached very quickly, in less than  $5 \cdot 10^4$  cycles. The surface plastic strain is much smaller than the strain applied during extrusion, and the change in the surface material is thus assumed to be negligible.

Concerning the fracture surface observations, fatigue crack initiation was always located on the surface of the specimen. Bending and tension specimens had the same type of fracture surfaces and in the majority of cases, the crack did not initiate on a surface defect or inclusion.

The crack profiles for each batch and loading condition are given in Fig. 13. Classically, the crack initiation in steel polycrystals

happens in the plane of maximum shear stress, which is angled at  $45^\circ$  from the loading direction, as observed by Morel and Huyen [17]. The crack then propagates perpendicular to the loading direction.

In our case, in tension, for all batches, the crack length in stage I (shear mode) of crack initiation and propagation is very small. The cracks propagate in the plane perpendicular to the loading direction and are perfectly linear before expanding in more jagged patterns due to the microstructure (Fig. 14). For the before extrusion batch, the crack stays mostly perpendicular to the loading direction, however for the extruded batches, the crack angles out after about 1 mm. The angle depends on the hardening, and reaches  $45^\circ$  for the 75% reduced cross-section batch. This is clearly visible on the fracture surfaces (Fig. 15), where the central part of the crack stays flat, and curves on the outer edges. For the 75% reduced cross-section specimens, the flat area is circular and easily distinguishable.

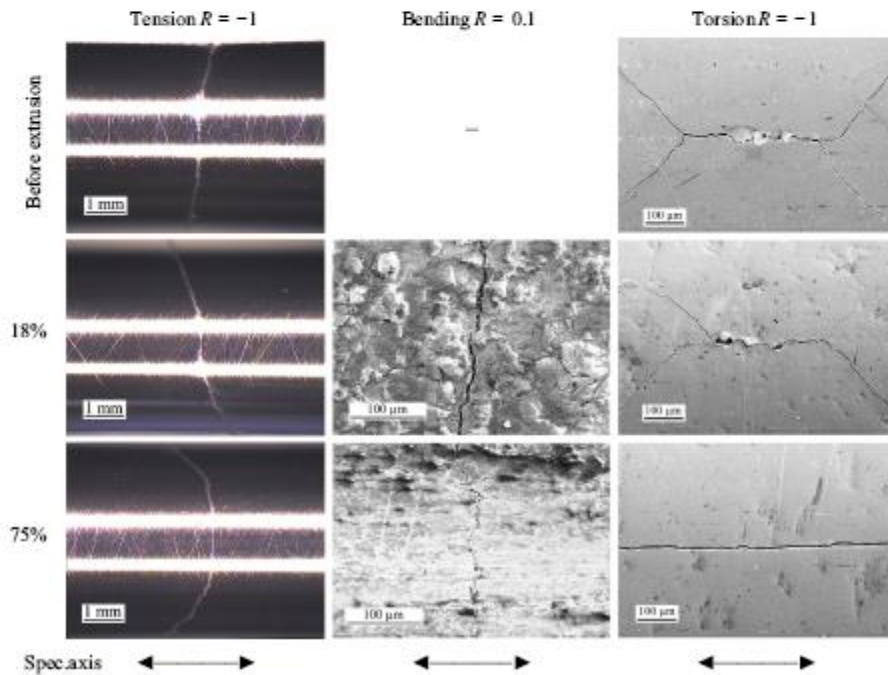


Fig. 13. Crack profiles for all batches. The bending and torsion profiles are SEM images.

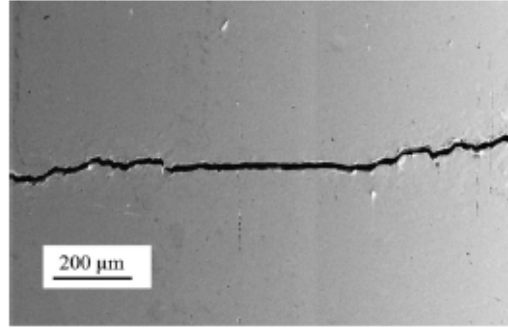


Fig. 14. SEM image of the crack profile of a 18% reduced cross-section fatigue specimen in tension. The loading direction is vertical.

In bending, the crack stays straight due to the specimen geometry and the machining marks from the milling prior to extrusion.

For the torsion tests, usually, the crack initiation and the persistent slip bands (PSB) are along both maximum stress planes, angled 0° and 90° [17]. In our case, both the PSB and the stage I crack are always parallel to the specimen axis. This is likely due to the ferrite and perlite bands present in the microstructure, which have the same orientation. The crack then follows the classical mechanism: the crack propagates several hundred microns in the maximum shear plane, before forking at a 45° angle (Fig. 13). For the extruded batches, the maximum shear plane has the same orientation as the microstructure and in the 75% reduced cross-section case, the microstructure keeps the crack at an 0° angle, even when reaching the specimen heads.

To conclude, the microstructure has two independent effects: the first is that the alternating ferrite and perlite bands make the stage I crack initiation always at 0°, and the second is that for the 75% reduced cross-section specimen, the highly anisotropic microstructure prevents the crack from forking. All these observations clearly show that the microstructure affects crack propagation.

## 5. Analysis

The tension fatigue tests with a load ratio  $R = -1$  were performed to investigate the influence of the prestrain on fatigue behaviour. The results of these tests show that hardening increases fatigue strength (Table 8), and that the increase in fatigue strength follows the same rate as the increase in ultimate strength. For all three batches, the ratio of the tension fatigue strength divided by the ultimate stress is always close to 0.40. This means that if the initial  $\sigma_{UTS}$  and fatigue strength are known, simply measuring the

Table 8

Fatigue and monotonic strength of the forged specimens. For bending, the values are the applied loading.

$\sigma$ (MPa)		Before extrusion	18%	75%
Tension	$\sigma_{UTS}$	691	768	1116
	$\sigma_e^{-1}$	252	303	461
Bending	$\sigma_e$	–	310	438
	$\sigma_m$	–	379	536
Torsion	$\tau_e^{-1}$	188	234	306
	$\sigma_e^{-1}/\sigma_{UTS}$ ratio	0.36	0.39	0.41
	$\tau_e^{-1}/\sigma_e^{-1}$ ratio	0.75	0.77	0.66

$\sigma_{UTS}$  is enough to predict the fatigue strength for other hardening levels. However this requires forging at least one specimen for the purpose of performing a tensile test, which can be very costly and time-consuming. Furthermore, for components with complex geometries and hardening gradients, the  $\sigma_{UTS}$  value cannot be easily measured.

A simpler method is to use the hardness value from FE simulations to predict the fatigue strength. An empirical law is sometimes used for steels:  $\sigma^B = 1.5 \times H_V$ , detailed by Garwood et al. [9] and taken up by other authors, such as Chapetti [3]. This model is quite accurate despite its simplicity, leading to a maximum error of 13% in our case (Fig. 16a). Using this approach with the hardness values from the previously discussed simulations leads to a prediction of the fatigue strength with an error of about 24% for the 18% reduced cross-section specimen (using the core hardness of 250  $H_V$ ) and an error of 2% for the 75% reduced cross-section specimen. The advantage of this method is that it can then be used to predict the local fatigue strength in a component with a heterogeneous hardness.

Some authors show that the Hall-Petch equation (based on the work of Hall [11] and Petch [28], used by Thompson [33]) can be used to link fatigue strength and grain size:

$$\sigma^B = A + \frac{B}{\sqrt{d}} \quad (2)$$

where  $A$  and  $B$  are constants and  $d$  is the grain size.  $A$  and  $B$  were determined by fitting the experimental data points using the method of least squares. The studied material exhibits a Hall-Petch tendency, when the transverse grain sizes are used (Fig. 16a). This model however requires at least two points (and thus two fatigue tests) for the constants to be fitted.

Since  $\sigma_{UTS}$  and fatigue strength are proportional, both of these methods can also be used to predict the  $\sigma_{UTS}$ . However, this type of approach should not be used when the damage mechanism changes with hardness, for example quenched steels, as shown by Pang et al. [24]. At low hardness, the crack initiation is mostly

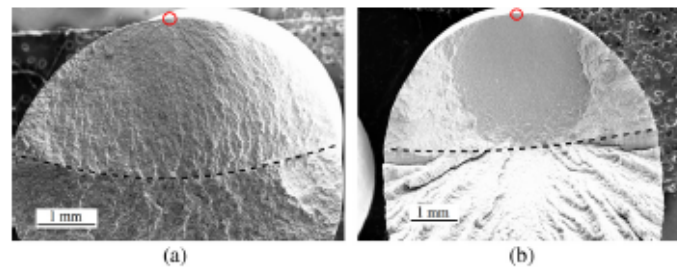


Fig. 15. Fracture surface in tension of: (a) 18% reduced cross-section specimen and (b) 75% reduced cross-section specimen. Crack initiation is located at the top (circle). The crack front at the end of the fatigue test is shown in dotted lines.

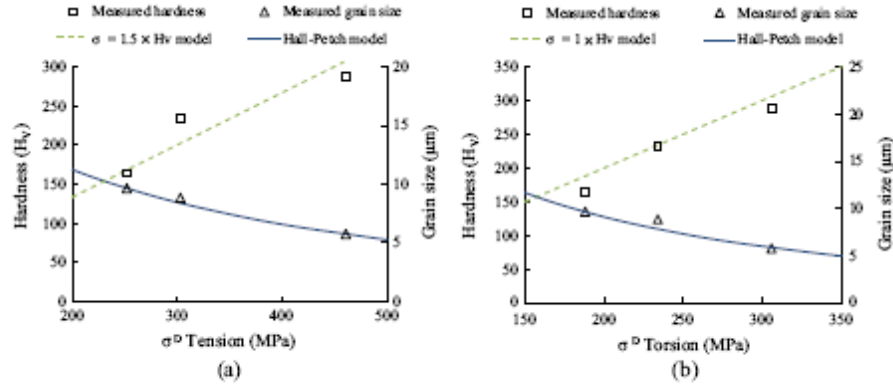


Fig. 16. Hardness and grain size according to the fatigue strength in (a) tension and (b) torsion. For torsion, the hardness model is simply  $\sigma^D = H_V$ .

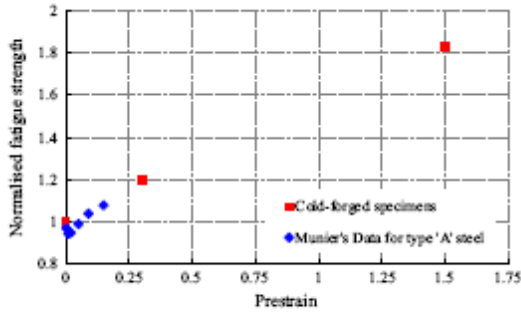


Fig. 17. Influence of prestrain on fatigue strength, comparing the fatigue results with data from Munier [18].

in the microstructure, but at very high hardness, the crack initiation tends to be located on inclusions.

When comparing the tension fatigue results with those of Munier [18], which are also in  $R = -1$  tension, the fatigue results seem to match the tendency exhibited by Munier's type "A" steel, which is a DP600 series steel (Fig. 17). However, it should be noted that the prestrain applied by Munier was in tension and thus different than our multiaxial compressive prestrain.

In addition to tension fatigue tests, bending tests were also performed to quantify the influence of the forged surface. During the fatigue tests, a small amount of plasticity affected the local residual stresses. To work with the correct local stress values, the loading

stress amplitude and the compressive residual stresses measured on the surface after fatigue cycling (on surviving specimens) are used. The stress amplitude is not affected by the residual stresses, thus the local stress amplitude is equal to the macroscopic (applied loading) stress amplitude. The local mean stress is the macroscopic mean stress with the (compressive) residual stresses added. The correct local fatigue strengths are given in Table 8.

These fatigue results can then be represented in a Haigh diagram (Fig. 18). Gerber [10] curves were used to represent the three batches. These curves are defined as:

$$\sigma_a = \sigma_a^{-1} \left( 1 - \left( \frac{\sigma_m}{\sigma_{UTS}} \right)^2 \right) \quad (3)$$

where  $\sigma_a$  is the loading stress amplitude,  $\sigma_a^{-1}$  is the fully reversed stress amplitude and  $\sigma_m$  is the mean stress. The effect of the prestrain can be clearly seen in the increase in the size of the curves, improving fatigue and tensile strength. The local (corrected) bending fatigue strengths are very close to the Gerber curves. This means that the fatigue behaviour is similar on the forged surface (bending tests) and at the core (tension tests) of the forged component. This is in agreement with the simulations and the hardness tests as they show little to no gradient along the depth of the specimens. Additionally, this means that the surface state produced during extrusion does not negatively impact the fatigue behaviour.

The last type of fatigue test performed were torsion  $R = -1$  tests (results in Table 8). The torsion fatigue strength varies almost linearly with the hardness (Fig. 16b), and also shows a direct link to the grain size. The shear/tension fatigue strength ratio is  $\tau_a/\sigma_a = 0.75$  before extrusion, which is a typical value for ductile steels, as shown by Pessard et al. [27].

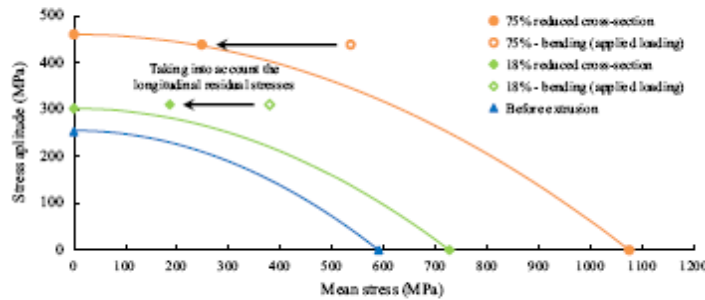


Fig. 18. Haigh diagram showing the results of the tension and bending fatigue tests, and the tensile tests.

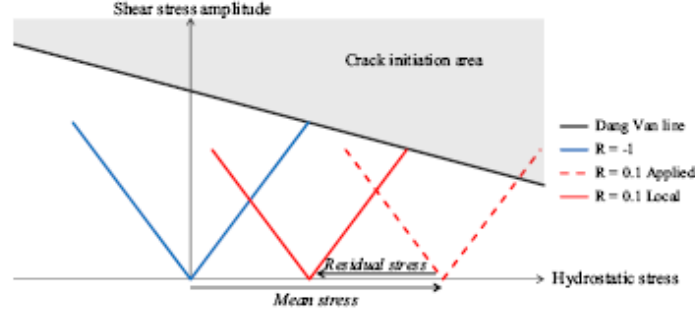


Fig. 19. Dang Van diagram showing the load path for uniaxial  $R = -1$  and  $R = 0.1$  loadings, and how the residual stresses are applied to obtain the local loading path.

The Dang Van [4] criterion can be used to take into account the different loading types. The advantage of this approach over the Haigh diagram is twofold: it defines a multiaxial fatigue criterion and it enables the correction of residual stresses in all directions. Indeed, on the forged surface, the residual stresses are not only in the extrusion direction, but also in the transverse direction (Table 7). Radial residual stresses are assumed equal to zero on the surface.

The Dang-Van criterion is written as follows:

$$\max_t [\tau(t) + \alpha \sigma_H(t)] = \beta \quad (4)$$

where  $\tau$  is the shear stress and  $\sigma_H$  is the hydrostatic stress, with  $\alpha$  and  $\beta$  material parameters. In the case of proportional loadings, the criterion can be simplified as:

$$\tau_a + \alpha \sigma_{Hmax} = \beta \quad (5)$$

where  $\tau_a$  is the time-dependant shear stress amplitude on a critical plane and  $\sigma_{Hmax}$  is the maximum hydrostatic stress. In a  $\tau$  versus  $\sigma_H$  diagram, the criterion defines a line of slope  $-\alpha$  which represents the maximum acceptable stress in fatigue (Fig. 19). If the loading path goes above this line, crack initiation occurs.

The hydrostatic stress  $\sigma_H$  can be broken down into loading amplitude, mean stress, and the residual stresses:

$$\sigma_H = \sigma_{HAmplitude} + \sigma_{HMean} + \sigma_{HResidual} \quad (6)$$

It is therefore simple to take into account the effects of residual stresses on the fatigue behaviour. By taking into account the residual stresses, the local stress loading is calculated, as opposed to the applied macroscopic loading. The time-dependent local stress tensors for each loading condition are written as:

$$\text{Tension : } [\sigma(t)] = \begin{pmatrix} \sigma_a & 0 & 0 \\ 0 & 0 & 0 \\ 0 & 0 & 0 \end{pmatrix} \sin(\omega t) \quad (7)$$

$$\text{Bending : } [\sigma(t)] = \begin{pmatrix} \sigma_a & 0 & 0 \\ 0 & 0 & 0 \\ 0 & 0 & 0 \end{pmatrix} \sin(\omega t) + \begin{pmatrix} \sigma_{mean} & 0 & 0 \\ 0 & 0 & 0 \\ 0 & 0 & 0 \end{pmatrix} + \begin{pmatrix} \sigma_{1Res} & 0 & 0 \\ 0 & \sigma_{2Res} & 0 \\ 0 & 0 & 0 \end{pmatrix} \quad (8)$$

$$\text{Torsion : } [\sigma(t)] = \begin{pmatrix} 0 & \tau_a & 0 \\ \tau_a & 0 & 0 \\ 0 & 0 & 0 \end{pmatrix} \sin(\omega t) \quad (9)$$

The resulting Dang-Van diagram is given in Fig. 20, where for the sake of clarity, each loading path in the diagram is represented by the single point in time where they are most critical. The slopes of the Dang-Van lines are very close for the before extrusion and the 18% reduced cross-section batches (0.76 and 0.77 respectively). The line for the 75% reduced cross-section specimens is slightly lower, at 0.52. Fig. 21 plots the  $\alpha$  and  $\beta$  values over the hardness. The  $\beta$  value is the torsion fatigue strength, which increases

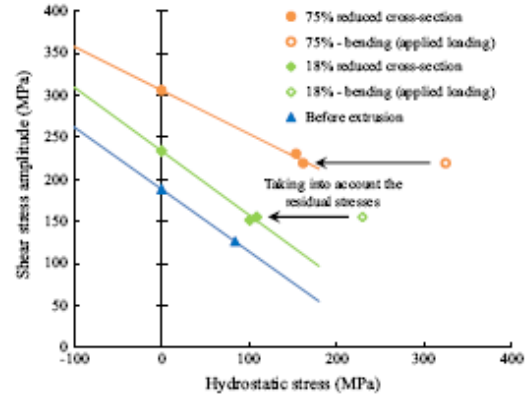


Fig. 20. Dang Van diagram showing the results of the fatigue tests.

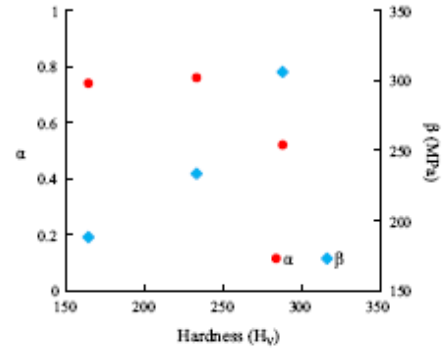


Fig. 21.  $\alpha$  and  $\beta$  values of the Dang Van criterion for the three batches Dang Van diagram showing the results of the fatigue tests.

Table 9  
Comparison of the  $\alpha$  value of the studied material with those of other materials from the literature.

Material	State	Hardness	$\tau_a^{-1}/\sigma_a^{-1}$	$\alpha$
27MnCr5	Before extrusion	164 Hv 0.2	0.75	0.76
	75%	288 Hv 0.2	0.66	0.52
22MnB5 Pessard et al. [27]	Initial state	180 Hv 20	0.69	0.57
	Quenched	600 Hv 20	0.82	0.96
XC18 Palin-Luc and Lasserre [23]	Annealed	–	0.68	0.54
FGS 800-2 Palin-Luc and Lasserre [23]	Cast iron	–	0.90	1.20

proportionately with hardness. The  $\alpha$  value represents the material's sensitivity to hydrostatic stress and varies with hardness. However, hardness is not the only parameter controlling the fatigue behaviour, the microstructure also has an effect on crack initiation and propagation. In our case, the increase in hardness and thus fatigue strength does not induce an increased fragility of the material (i.e. an increased sensitivity to hydrostatic stress, represented by higher  $\alpha$  values). This is contrary to the classical tendency observed in certain heat-treated materials by Palin-Luc and Lasserre [23]. Table 9 compares our  $\alpha$  and  $\tau_a^{-1}/\sigma_a^{-1}$  values with those of heat-treated steels from the literature. When the increase in hardness comes from hardening, the higher hardness does not increase the material's sensitivity to hydrostatic stress. For the heat-treated steels, the increased hardness is detrimental and makes the material more fragile (more sensitive to hydrostatic stress). It should be noted however, that the hardness values are very different between cold-forged and heat-treated, and that the increased fragility could be observed only for extreme hardness values.

All the results presented here confirm the observations found in the literature and quantify the influence of prestrain on fatigue behaviour. The range of the prestrain values studied is quite large, with a very high maximum value.

In addition to the fatigue tests detailed here and mainly focused on the initiation phase of the fatigue damage behaviour, another study on the influence of prestrain on the crack propagation rate, using synchrotron tomography, is in progress and will be detailed in a companion paper.

## 6. Conclusion

In this study, fatigue tests and material characterisation were conducted on specimens with two different amounts of prestrain and on the initial material. The specimens were cold-forged with a reduction of the cross section of 18% and 75%, leading to equivalent plastic strains of 0.3 and 1.5 respectively. The fatigue tests were performed in tension, bending and torsion. Using the results of these tests, it was possible to take into account the most important process parameters in cold-extrusion (hardening and residual stresses) which can affect the multiaxial fatigue behaviour. The main conclusions of this study are:

- Hardening through extrusion increases the fatigue strength for all tested loading conditions (tension, bending and torsion).
- Fatigue behaviour for the surface and the core material are the same.
- Fatigue strength can be linked to the hardness value, and the hardness can be reasonably predicted through FE simulations.
- The various fatigue tests taken together enable the use of a multiaxial fatigue criterion.
- The crack path is affected by the microstructure, especially for the batch with 75% reduced cross-section.
- The hardening introduced by process does not render the material more sensitive to hydrostatic stress.

This work is part of an overall approach, the goal of which is to improve the prediction of the fatigue strength through the development of a complete numerical chain. This would allow the integration of the results of the FE simulation of the process into the fatigue design of components.

After having shown in previous studies that it is possible, and worthwhile, to take into account the fibering [25,26], the present article focuses on the effect of prestrain on the fatigue behaviour of forged components.

## Acknowledgements

This work has been performed within the ANR (National Research Agency) DEFISURF project, in a partnership including several industrial (Ascometal, Cetim, PSA, Transvalor, Atelier des Javes, Gévelot) and academic (INSA Lyon MATEIS, ENSMP-CMEF, Arts et Métiers ParisTech LAMPA) institutions.

## References

- [1] Beretta S, Boniardi M. Fatigue strength and surface quality of eutectoid steel wires. *Int J Fatigue* 1999;21(4):329–35.
- [2] Bouchard P, Laurent T, Tollier L. Numerical modeling of self-pierce riveting – from riveting process modeling down to structural analysis. *J Mater Process Technol* 2008;202(1–3):290–300.
- [3] Chapetti MD. A simple model to predict the very high cycle fatigue resistance of steels. *Int J Fatigue* 2011;33(7):833–41.
- [4] Dang-Van K. Macro-micro approach in high-cycle multiaxial fatigue. *Proceedings of advances in multiaxial fatigue, ASTM STP* 1993;1191:120–30.
- [5] Dixon WJ, Mood AM. A method for obtaining and analyzing sensitivity data. *J Am Stat Assoc* 1948;43:109–26.
- [6] Felner CE, Laird C. Cyclic stress-strain response of F.C.C. metals and alloys-I. Phenomenological experiments. *Acta Metall* 1967;15(10):1621–32.
- [7] Froustey C, Lataillade JL. Influence of large pre-straining of aluminium alloys on their residual fatigue resistance. *Int J Fatigue* 2008;30(5):908–16.
- [8] Gariety M, Ngalle G, Altan T. Evaluation of new cold forging lubricants without zinc phosphate precoat. *Int J Mach Tools Manuf* 2007;47(3–4):673–81.
- [9] Garwood M, Gensamer M, Zurburg H, Burwell J, Erickson M, La Que F. Interpretation of tests and correlation with service. *American Society for Metals* 1951.
- [10] Gerber WZ. Bestimmung der zulässigen spannungen in eisenconstructionen. *Zeitschrift des Bayerischen Architekten und Ingenieur-Vereins* 1874;6(6):101–10.
- [11] Hall EO. The deformation and ageing of mild steel – III discussion of result. *Proc Phys Soc London, Sect B* 1951;64(9):747–53.
- [12] Kang M, Aono Y, Noguchi H. Effect of prestrain on and prediction of fatigue limit in carbon steel. *Int J Fatigue* 2007;29(9–11):1855–62. [Fatigue Damage of Structural Materials VI. The Sixth International Conference on Fatigue Damage of Structural Materials].
- [13] Kunz L, Lukš P, Weiss B, Melisova D. Effect of loading history on cyclic stress-strain response. *Mater Sci Eng A* 2001;314(1–2):1–6.
- [14] Libertini G, Topper T, Leis B. The effect of large prestrains on fatigue. *Exp Mech* 1977;17(2):64–8.
- [15] Marnier G, Keller C, Lakhdar Taleb L. Tensile prestrain memory effect on subsequent cyclic behavior of (FCC) metallic materials presenting different dislocations slip modes. *Int J Plast* 2016;78:64–83.
- [16] Maxwell DC, Nicholas T. A rapid method for generation of a Haigh diagram for high cycle fatigue. In: Panonon TL, Sheppard SD, editors. *Fatigue and fracture mechanics. ASTM STP* 1321, vol. 29. West Conshohocken (PA): American Society for Testing and Materials; 1999. p. 626–41.
- [17] Morel F, Huyen N. Plasticity and damage heterogeneity in fatigue. *Theoret Appl Fract Mech* 2008;49(1):98–127.

- [18] Munier R. Etude de la fatigue des aciers laminés à partir de l'autoéchauffement sous sollicitation cyclique: essais, observations, modélisation et influence d'une pré-déformation plastique, s.l.: PhD ENSTA-Bretagne; 2012.
- [19] Munier R, Doudard C, Calloch S, Weber B, Facchinetti M. Contribution of kinematical and thermal full-field measurements for mechanical properties identification: application to high cycle fatigue of steels. *Exp Mech* 2012;52(7):743–56.
- [20] Murakami Y. Metal fatigue: effects of small defects and nonmetallic inclusions. London: Elsevier; 2002.
- [21] Nagase Y, Suzuki S. On the decrease of fatigue limit due to small prestrain. *J Eng Mater Technol* 1992;114(3):317–22.
- [22] Pale JA, Shivpuri R, Altan T. Recent developments in tooling, machines and research in cold forming of complex parts. *J Mater Process Technol* 1992;33(1–2):1–29.
- [23] Palin-Luc T, Lasserre S. An energy based criterion for high cycle multiaxial fatigue. *Eur J Mech A Solids* 1998;17(2):237–51.
- [24] Pang JC, Li SK, Wang ZG, Zhang ZF. General relation between tensile strength and fatigue strength of metallic materials. *Mater Sci Eng: A* 2013;564(0):331–41.
- [25] Pessard E, Morel F, Milesi M, Bouchard P, Ducoux R. A new methodology for designing forged components in fatigue. *Fatigue Design* 2009, CETIM; 2009.
- [26] Pessard E, Morel F, Bellett D, Morel A. A new approach to model the fatigue anisotropy due to non-metallic inclusions in forged steels. *Int J Fatigue* 2012;41:168–78.
- [27] Pessard E, Abrivard B, Morel F, Abroug F, Delhay P. The effect of quenching and defects size on the HCF behaviour of boron steel. *Int J Fatigue* 2014;68(0):80–9.
- [28] Petch NJ. The cleavage strength of polycrystals. *J Iron Steel Inst* 1953;174:25–8.
- [29] Pippan R. Threshold and effective threshold of fatigue crack propagation in ARMCO iron: the influence of grain size and cold working. *Mater Sci Eng A* 1991;138(1):1–13.
- [30] Sonmez F, Demir A. Analytical relations between hardness and strain for cold formed parts. *J Mater Process Technol* 2007;186(1–3):163–73.
- [31] Tabor D. The physical meaning of indentation and scratch hardness. *Br J Appl Phys* 1956;7(5):159–66.
- [32] Telkkaya A, Lange K. An improved relationship between vickers hardness and yield stress for cold formed materials and its experimental verification. *CIRP Ann – Manuf Technol* 2000;49(1):205–8.
- [33] Thompson A. The influence of grain and twin boundaries in fatigue cracking. *Acta Metall* 1972;20(9):1085–94.
- [34] Toribio J, González B, Matos J. Fatigue and fracture paths in cold drawn pearlitic steel. *Eng Fract Mech* 2010;77(11):2024–32 [International conference on crack paths 2009].
- [35] Wang Y, Yu D, Chen G, Chen X. Effects of pre-strain on uniaxial ratcheting and fatigue failure of Z2CN18.10 austenitic stainless steel. *Int J Fatigue* 2013;52:106–13.
- [36] Zimmermann M, Stöcker C, Müller-Bollenhagen C, Christ H-J. Prehistory effects on the VHCF behaviour of engineering metallic materials with different strengthening mechanisms. *J Phys: Conf Ser* 2010;240(1) [15th international conference on the strength of materials (ICSMA-15)].